



Evaluation of optimally windowed chirp signals in industrial rheological measurements: method development and data processing

Alessandro Perego¹ · Damien C. Vadillo¹ · Matthew J. L. Mills¹ · Mohua Das² · Gareth H. McKinley FRS²

Received: 14 May 2025 / Revised: 1 July 2025 / Accepted: 6 July 2025 / Published online: 15 August 2025
© The Author(s), under exclusive licence to Springer-Verlag GmbH Germany, part of Springer Nature 2025

Abstract

The optimally windowed chirp (OWCh) methodology offers an alternative to traditional discrete frequency sweeps, acquiring complete rheological spectra in seconds while preserving data density and accuracy. For thermorheologically simple materials, OWCh accelerates data collection, enabling rapid creation of time–temperature superposition (tTS) master curves, potentially saving hours of instrument time. For mutating materials, such as those undergoing curing, OWCh facilitates detailed rheological characterization of viscoelastic properties throughout these transition events. We implemented OWCh within an industrial analytical research framework using commercially available rheometers. This integration is enhanced by two custom Python packages, piblin and hermes-rheo, which streamline and automate analysis of rheological datasets. For thermorheologically simple materials, this framework reduces tTS master curve data collection time by 40% while increasing data density by an order of magnitude. For mutating materials, we leverage the mutation number to design OWCh waveforms, effectively probing the characteristic timescale of fast thermomechanical transitions during curing experiments.

Keywords Optimally windowed chirp (OWCh) · High-throughput rheological characterization · Data-driven rheology

Introduction

The characterization of material properties through rheological measurements is essential for understanding the behavior of complex fluids and soft materials undergoing deformation, especially in industrial and biomedical applications

(Mezzenga et al. 2005; Chen et al. 2010). Traditional rheometric techniques, such as discrete frequency sweeps (DFS), remain the cornerstone for linear viscoelastic characterization but are often time-consuming and inadequate for capturing transient behaviors in rapidly mutating systems (Totosaus et al. 2002; Leocmach et al. 2014). To address these limitations, frequency-modulated methods, including multi-wave (MW) (Winter and Chambon 1986; Ross-Murphy 1994), optimal Fourier rheometry (OFR), and chirp techniques (Ghiringhelli et al. 2012; Wilhelm 2002), have been developed. Among these, chirp signals—particularly the optimally windowed chirp (OWCh)—represent a significant advancement due to their ability to minimize spectral leakage and improve data accuracy across a broad frequency range (Geri et al. 2018; Müller 2001; Athanasiou et al. 2024; Rathinraj et al. 2022).

Chirp signals are frequency-modulated deterministic inputs in which the frequency varies continuously with time, inspired by echolocation mechanisms observed in nature (Au and Simmons 2007; Madsen and Surlykke 2013). Their low crest factor—defined as the ratio of the signal's peak amplitude to its root-mean-square (RMS) amplitude—combined with a high signal-to-noise ratio (SNR) and a periodic structure at the signal boundaries, makes them particularly advan-

Alessandro Perego and Damien C. Vadillo contributed equally to this work.

✉ Alessandro Perego
aperego@mmm.com

Damien C. Vadillo
dvadillo@mmm.com

Matthew J. L. Mills
mmills2@mmm.com

Mohua Das
mohuadas@mit.edu

Gareth H. McKinley FRS
gareth@mit.edu

¹ Corporate Research Analytical Laboratory, 3M, Maplewood 55144, MN, USA

² Department of Mechanical Engineering, Massachusetts Institute of Technology, Cambridge 02139, MA, USA

tageous for mechanical spectroscopy (Ghiringhelli et al. 2012; Wilhelm 2002; Geri et al. 2018). Unlike MW methods, which can risk exceeding the linear viscoelastic limit through additive superposition of multiple frequencies (Ghiringhelli et al. 2012), or OFR techniques, which may introduce spectral artifacts such as Fresnel ripples (Kowatsch and Stocker 1982), OWCh signals are specifically designed to mitigate these issues through judicious amplitude modulation and tapering (Müller 2001; Geri et al. 2018). These optimal features enable the precise determination of viscoelastic spectra which significantly reduce acquisition times compared to traditional frequency sweeps (Geri et al. 2018; Bouzid et al. 2018).

The OWCh methodology is particularly well suited for studying mutating systems, such as polymeric and colloidal gels undergoing gelation or phase transitions (Trappe and Weitz 2000; Zaccarelli 2007). These systems present unique challenges due to their evolving microstructure and the rapid time scales associated with their mutation dynamics (Chen et al. 2010). By monitoring the dynamic evolution of the mutation number during a test, OWCh signals of varying duration enable real-time adjustment of the input signal, allowing capture of frequency-dependent viscoelastic data that would otherwise remain inaccessible using conventional methods (Geri et al. 2018). Additionally, bias correction techniques enhance the fidelity of the measurements by addressing intrinsic noise, further improving data quality (Bouzid et al. 2018).

In this work, we implement the OWCh protocol within an industrial research framework and demonstrate its capability for accurately characterizing the rheology of both non-mutating and mutating materials. Specifically, we validate and optimize the OWCh methodology from analytical and data processing perspectives. Analytical improvements include refined waveform designs and advanced bias correction protocols that reduce measurement artifacts and significantly enhance the accuracy of viscoelastic measurements. Concurrently, robust data processing workflows have been established through the development of custom Python packages `piblin` (Mills et al. 2024) and `hermes-rheo` (Perego et al. 2024). These packages facilitate efficient data processing, visualization, and rapid generation of high-resolution master curves from complex rheological datasets.

These methodological advancements lead directly to two key outcomes. First, for non-mutating materials, we achieve substantial efficiency improvements in the acquisition of viscoelastic data, demonstrated by a 40% reduction in the total experimental test duration combined with an order-of-magnitude increase in frequency-domain data density compared to traditional discrete frequency sweeps. Second, for mutating materials, OWCh enables detailed, time-resolved rheological characterization, capturing the rapid evolution of viscoelastic properties during processes such as curing.

These enhancements provide clear guidelines for end-users seeking rapid, high-fidelity rheological data acquisition and offer instrument manufacturers concrete strategies for integrating OWCh techniques into next-generation rheometer hardware and software platforms.

Materials and methods

Materials

Two material systems were utilized in this study: (i) a commercially available adhesive tape and (ii) a thermally non-reversible, UV-curable acrylate system. The adhesive system employed was 3M™ High-Strength Acrylic Adhesive 300LSE specifically designed for applications requiring strong adhesion to high surface energy substrates (3M n.d.). The UV-curable acrylate system was formulated using equal weight fractions of bisphenol A diglycidyl ether, 3,4-epoxycyclohexylmethyl 3,4-epoxycyclohexanecarboxylate, and Voranol 220—a homopolymer diol (Dow n.d.). To facilitate UV-induced curing, the formulation incorporated the photoinitiator camphorquinone, along with ethyl 4-dimethylaminobenzoate as an amine synergist and 4-isopropyl-4'-methyldiphenyliodonium tetrakis(pentafluorophenyl) borate as a photoacid. The resin components were mixed thoroughly at room temperature to ensure uniformity prior to testing.

Experimental setup

The rheological experiments were performed in strain-controlled mode on a TA® Instruments ARES-G2 rheometer under sample- and temperature-specific protocols. For the non-mutating 3M™ High-Strength Acrylic Adhesive, a ~ 1 mm-thick sample was prepared by stacking multiple layers of adhesive, then punching out a series of 8 mm diameter disks. Testing was conducted in air with an 8 mm parallel-plate geometry, and temperatures ranged from –40 to 150°C, in 10°C increments. Although rheometric studies of polymer viscoelasticity are often performed under a nitrogen purge to mitigate oxidative degradation, the material studied here is thermally stable up to approximately 300°C, so no inert atmosphere was required. Each isothermal step was held for 3 min of equilibration before performing discrete frequency sweeps (DFS) spanning $0.6 \leq \omega \leq 125$ rad/s at seven points per decade (17 total frequency points per sweep).

For the UV-curable acrylate system, experiments were carried out at 20°C using a Peltier-controlled stage coupled with a 20-mm transparent, disposable top plate made of acrylate. UV illumination was provided by a 10 W/cm² Excelitas Omnicure® LX500 LED source operated at 60% power. Prior to each test, the lamp output was calibrated to

account for transmittance variations through the top plate. The sample gap was 0.5 mm. Due to the rapid reaction kinetics of the UV-curable system, it was impossible to perform full DFS measurements. Instead, the sample characterization was limited to a time sweep at a single fixed frequency of $\omega = 2\pi$ rad/s. In contrast, the frequency-modulated OWCh approach employed a sampling frequency of 1000 pts/s with a 1 s waiting time (t_w) over a total chirp duration, T_{owc} , of 14 s. The imposed frequency range extended from $\omega_1 = 0.3$ rad/s to $\omega_2 = 60$ rad/s with a tapering coefficient of $r = 0.05$ (see Geri et al. 2018 for details), giving a time-bandwidth product $TB = T_{owc}(\omega_2 - \omega_1)/2\pi = 133$. These conditions were selected to balance temporal and spectral resolution for both test samples. For the UV-curable acrylate, the OWCh frequency range was later reduced to shorten the signal duration to less than 14 s in order to accommodate short mutation timescales, as discussed in Sect. 3.3.

OWCh waveform design

Accurate viscoelastic characterization within the linear deformation regime is critical in many research and development activities. In conventional small amplitude oscillatory shear (SAOS) tests, the storage modulus G' and loss modulus G'' are determined via discrete frequency sweeps (DFS). In these tests, a sinusoidal signal

$$x(t) = x_0 \sin(\omega t) \quad (1)$$

(with x_0 representing either the stress or strain amplitude and ω the angular frequency) is applied sequentially at a series of fixed frequencies and the output amplitude and phase-shift is measured. Regardless of whether the test is stress- or strain-controlled, the complex modulus is obtained in the frequency domain via Fourier transformation:

$$G^*(\omega) = \frac{\tilde{\sigma}(\omega)}{\tilde{\gamma}(\omega)}, \quad (2)$$

where $\tilde{\sigma}(\omega)$ and $\tilde{\gamma}(\omega)$ are the Fourier transforms of the time-domain stress, $\sigma(t)$, and strain, $\gamma(t)$, respectively. The storage and loss moduli are then given by

$G'(\omega) = \Re\{G^*(\omega)\}$ and $G''(\omega) = \Im\{G^*(\omega)\}$, where \Re and \Im denote the real and imaginary parts.

For each discrete input pair (x_0, ω) , the data collection time is approximately $\frac{2\pi}{\omega}$ (or higher if multiple cycles are acquired). Consequently, the total duration of a DFS is given by the following:

$$T_{DFS} \geq \sum_{i=1}^m \frac{2\pi}{\omega_i}, \quad (3)$$

where m is the number of tested frequencies. The recently introduced OWCh method by Geri et al. (2018) offers a compelling alternative by significantly reducing the total data acquisition time.

In an exponential chirp (Ghiringhelli et al. 2012), the excitation signal is modified with an exponentially increasing frequency modulation, given by

$$\omega(t) = \omega_1 \left(\frac{\omega_2}{\omega_1} \right)^{\frac{t}{T_{owc}}}, \quad (4)$$

where ω_1 and ω_2 are the lower and upper bounds of the frequency interval (in rad/s), and T_{owc} is the total duration of the chirp.

The chirp is generated by applying the frequency sweep to a constant-amplitude sinusoid, which is then windowed using a cosine-tapered (Tukey) function (Harris 2005) to suppress nonlinear responses at high frequencies. The resulting OWCh waveform is thus defined as

$$x(t) = x_0 \begin{cases} \cos^2 \left[\frac{\pi}{r} \left(\frac{t - t_w}{T_{owc}} - \frac{r}{2} \right) \right] \sin \left\{ \frac{\omega_1 T_{owc}}{\ln(\omega_2/\omega_1)} \left[\exp \left(\frac{\ln(\omega_2/\omega_1)}{T_{owc}} (t - t_w) \right) - 1 \right] \right\}, & \frac{t - t_w}{T_{owc}} \leq \frac{r}{2}, \\ \sin \left\{ \frac{\omega_1 T_{owc}}{\ln(\omega_2/\omega_1)} \left[\exp \left(\frac{\ln(\omega_2/\omega_1)}{T_{owc}} (t - t_w) \right) - 1 \right] \right\}, & \frac{r}{2} \leq \frac{t - t_w}{T_{owc}} \leq 1 - \frac{r}{2}, \\ \cos^2 \left[\frac{\pi}{r} \left(\frac{t - t_w}{T_{owc}} - 1 + \frac{r}{2} \right) \right] \sin \left\{ \frac{\omega_1 T_{owc}}{\ln(\omega_2/\omega_1)} \left[\exp \left(\frac{\ln(\omega_2/\omega_1)}{T_{owc}} (t - t_w) \right) - 1 \right] \right\}, & \frac{t - t_w}{T_{owc}} \geq 1 - \frac{r}{2}, \end{cases} \quad (5)$$

In Eq. (5), the duration T_{owc} is chosen based on the lowest frequency such that $T_{owc} \geq \frac{2\pi}{\omega_1}$. Using the shortest possible OWCh reduces the number of free parameters. For example, for a lower frequency bound of 0.3 rad/s, one obtains $T_{owc} \sim 21$ s.

To improve experimental throughput for internal applications, we adopted a practical convention in which the OWCh duration is shortened to two-thirds of the theoretical minimum, i.e., $T_{owc} \geq \frac{2}{3} \cdot \frac{2\pi}{\omega_1}$. This choice reduces the acquisition time by approximately 33% while only modestly shifting the lowest reliably probed frequency (e.g., from 0.3 to approximately 0.45 rad/s). Although this $\frac{2}{3}$ scaling factor is not theoretically required, it was selected to balance test duration

with frequency resolution in routine workflows. This design decision is consistently applied in both waveform generation and data processing throughout the present study. This minor reduction in data points enables a substantial decrease in total acquisition time, significantly enhancing experimental efficiency.

Figure 2a presented below illustrates a representative OWCh waveform, showing both the input strain (γ) and output stress (σ) signals. The tapering parameter r corresponds to the Tukey window's cosine fraction (see Eq. 5), with values between 5 and 15% found to be optimal (Geri et al. 2018).

Implementation of OWCh

A TA Instruments™ ARES-G2 rheometer using the TRIOS software can be programmed to perform OWCh experiments via the Arbitrary Waveform method. In this approach, users must supply up to four distinct equations that describe the OWCh waveform (TA Instruments 2014). To streamline this process, the `hermes-rheo` package (discussed in Sect. 3) provides an automated solution through the `OWChGeneration` transform, which generates all necessary waveform parameters. A tutorial can be found in the `hermes-rheo` software repository (Perego 2024a).

The wave design tool allows for an optional waiting time $t_w > 0$ parameter to be inserted at the start or at the end of the OWCh wave. Although not strictly required, this waiting time ultimately improves data quality by capturing and removing any systematic signal bias or sudden optical encoder shifts at the commencement of the measurement. The data acquired during this initial waiting period are used to quantify and eliminate these offsets, ensuring that the time-varying input and output signals are symmetric about zero (i.e., starting and ending at zero and oscillating evenly about zero) prior to FFT processing. Failure to account for these effects can lead to spectral leakage, manifesting as artificial modulations in the elastic and loss moduli or increased noise at high frequencies.

OWCh parameter selection

The implementation of an OWCh experiment via the arbitrary waveform (AW) method requires the definition of a set of equations that describe the rheometer's strain or stress input. The rheometer software then samples these equations to construct a discretized waveform trajectory as a function of time. This digitization process varies across instruments and is constrained by the available memory, which limits the number of discrete data points, N . Consequently, the OWCh design constraints, particularly the OWCh duration (T_{owc}) and upper frequency (ω_2), must be carefully chosen to ensure a smooth waveform with well-defined maxima.

The interplay between key input parameters is captured by the normalized Nyquist number (Nyquist 1928; Landau

1967):

$$N_y = \frac{(T_{\text{owc}} + t_w)\omega_2}{2\pi N}, \quad (6)$$

where T_{owc} is the total OWCh duration, t_w is the waiting time, and ω_2 is the final angular frequency of the OWCh signal. The Nyquist-Shannon sampling theorem (Shannon 1949) states that the minimum required sampling frequency must be at least twice the highest probed frequency, i.e.,

$$\min\{f_s\} > \frac{2\omega_2}{2\pi}. \quad (7)$$

Since the total number of sampling points is related to the sampling frequency via $f_s(T_{\text{owc}} + t_w) = N$, substituting into Eq. (6) yields the condition $N_y \leq 0.5$. However, while this criterion is theoretically sufficient, in practice, an OWCh signal sampled at this rate may exhibit aliasing, particularly when $\omega_2 \geq 60$ rad/s. To mitigate undersampling artifacts, Hudson-Kershaw et al. (2024) proposed a more stringent constraint. In this study, we set $N_y < 0.1$, which translates to a modified Nyquist condition requiring:

$$\frac{10\omega_2}{2\pi} \leq f_s \leq \frac{N_{\max}}{T_{\text{owc}} + t_w}, \quad (8)$$

where N_{\max} represents the maximum number of recordable points allowed by the rheometer's memory. The lower bound ensures adequate frequency resolution, while the upper bound prevents data overflow.

For example, considering experimental conditions for which $\omega_1 = 0.3$ rad/s, $\omega_2 = 125$ rad/s, $T_{\text{owc}} = 14$ s, and $t_w = 1$ s, performed on a TA ARES-G2 rheometer with $N_{\max} = 2^{15}$, Eq. (8) yields a valid sampling range of $200 \text{ pts/s} \leq f_s \leq 2184 \text{ pts/s}$.

As mentioned in the previous section, spectral leakage can introduce unwanted side lobes in the power spectra of both the input and output signals. These artifacts can be minimized if the time-bandwidth product satisfies the conservative estimate $TB \geq 100$, as suggested by Geri et al. (2018). However, empirical studies by the same authors indicate that high-quality OWCh data can still be obtained even for $TB \approx 66$. A comprehensive discussion on the proper selection of input parameters for OWCh testing has been presented by Hudson-Kershaw et al. in the form of a method design space diagram (see Fig. 7 in Hudson-Kershaw et al. (2024)).

Despite these constraints, it is not always possible to simultaneously optimize both N_y and TB . In such cases, priority should be given to ensuring sufficient sampling density (i.e., satisfying $N_y < 0.1$) rather than strictly enforcing $TB \geq 100$. This trade-off becomes particularly relevant when studying mutating systems, in which the timescale of interest is dictated by the time evolving viscoelastic properties.

ties of the sample. The characteristic mutation time τ_{Mu} is defined as follows:

$$\tau_{Mu} = \left[\frac{d \ln g}{dt} \right]^{-1}, \quad (9)$$

where g represents any relevant viscoelastic quantity (Mours and Winter 1994). To ensure that viscoelastic measurements remain valid, the OWCh input duration must be adjusted such that the sample remains in a quasi-static state during data acquisition. This condition is typically satisfied when the dimensionless mutation number, defined as follows:

$$Mu = \frac{T_{owc}}{\tau_{Mu}}, \quad (10)$$

does not exceed $Mu \leq 0.15$ (Mours and Winter 1994; Curtis et al. 2015).

As previously discussed, the OWCh technique can only be implemented via rheometer programming. One direct implication is that the user must manually regulate the input signal amplitude to ensure that the output signal remains within the expected range. While this is straightforward for single OWCh tests, experiments involving multiple temperature sweeps or mutating materials require significantly more effort to design, implement, and optimize. In our experience, this often necessitates trial-and-error adjustments, complementary validation tests, or interpolation-based optimization to determine the appropriate input boundaries.

Finally, it is important to note that frequency-modulated methods inherently yield a higher data density compared to traditional discrete frequency approaches. The relationship between the OWCh input parameters and the number of data points measured in the frequency domain, N_f , can be calculated as follows:

$$N_f = \frac{2^n(\omega_2 - \omega_1)}{2\pi f_s}, \quad (11)$$

where 2^n is the number of time-domain points collected over the total signal duration T_{owc} , rounded up to the nearest power of two for efficient processing using the fast Fourier transform (FFT) algorithm (Nussbaumer 1982). As a practical example, an OWCh signal comprising 15,999 time-domain points sampled at 1000 pts/s (see Fig. 2a) generates 78 frequency-domain data points within the 0.3–30 rad/s range. In contrast, a conventional discrete frequency sweep might collect only 5–10 frequency points per decade over the same interval. Consequently, OWCh delivers an order-of-magnitude increase in spectral resolution while simultaneously reducing the overall testing duration.

Data processing

All data presented in this study were processed using two Python packages developed at 3M™, `piblin` (Mills et al. 2024) and `hermes-rheo` (Perego et al. 2024), both of which are distributed under the MIT open-source license. The name `piblin` originates from the Cymraeg word for “pipeline,” reflecting its role as a comprehensive framework for reading, representing, transforming, and visualizing measurement data within cohesive data pipelines. This package provides fundamental abstractions upon which data processing pipelines for any analytical technique can be implemented with minimum effort and then integrated into scripts, computational notebooks, and user interfaces with ease. Building upon `piblin`’s core functionalities, `hermes-rheo`—so named for the swift messenger of the Greek pantheon—provides advanced rheological data transformations specifically tailored to high-throughput needs.

Originally developed to facilitate the analysis of OWCh experiments, `hermes-rheo` has evolved into a universal rheological toolkit that supports commonly used rheological procedures (e.g., discrete frequency sweeps, stress relaxation, creep) as well as novel analytical methods. One of its primary advantages for OWCh analysis is an automated bias correction protocol, which builds upon and extends the bias correction methodologies discussed by Geri et al. (2018). Specifically, `hermes-rheo` applies an automated procedure which systematically applies three distinct filtering methods—subtracting the average calculated from (i) only the waiting-time interval, (ii) only the OWCh segment, or (iii) the entire signal duration. The corrected signals from each approach are evaluated based on symmetry around zero and minimal deviations at their starting and ending points, ensuring that signals both begin and end at zero. The algorithm then automatically selects the optimal filtering method that best meets these criteria, effectively eliminating systematic errors such as residual motor offsets and torque transducer drift without manual intervention, thus ensuring consistently accurate and repeatable viscoelastic measurements.

While existing MATLAB™ tools such as MIT OWCh V1.01 (Geri et al. 2018) and SUMIT OWCh (Curtis et al. 2015) have offered valuable insights in academic settings, their focus on academic applications and inherent software licensing costs limit their scalability for industrial use. In contrast, the modular Python packages `piblin` and `hermes-rheo` (distributed under the MIT Open-source license) have intentionally been developed so that they can be freely used in diverse contexts. At its simplest, an individual user may directly use the software to perform analysis of data on a personal laptop. At the other extreme, it is straightforward to incorporate the `hermes-rheo` package into fully automated cloud-based data analysis pipelines. The modular nature of the packages allows their elements to be used as

building blocks for integrating OWCh measurements with complementary characterization methods. The open-source, extensible framework allows users to tailor the workflow to their specific research or production needs, thereby ensuring efficient, comprehensive, and cost-effective rheological analysis at scale.

Figure 1 shows how these tools can be incorporated into an automated, cloud-based system for data analysis and reporting. At the core of this schematic is the collection of data by analytical scientists, which in some cases may include both automated sample preparation and/or loading. The raw data produced is detected, moved to cloud storage, and indexed within a data mesh ecosystem by a fully automated application. The raw data may be further automatically processed, and then raw and processed output can be both formatted for human interpretation and also stored in structured databases. The latter enables historical analyses, including both keyword and content-based retrieval in perpetuity, while the large datasets that result can feed big data, AI and digital twin approaches. The processed output data provides near-immediate insight into the evolving rheological properties of thermally sensitive or curing samples, which coupled with advanced techniques like OWCh is potentially transformational in terms of speed and data density for industrial research and development. Search, visualization, manual processing, and interpretation tools are also deployed as

cloud applications, hugely easing data governance concerns by allowing all data access management to depend on a central corporate system and maintaining the integrity of raw data through its maintenance in a central location. Throughout the system, core functionality provided by the described Python packages is easily accessible through Python's package management system. Many of these now-automatic steps are currently manual in industrial environments, and systems such as those schematized in Fig. 1 represent a significant shift towards digital transformation and provide a path to digital integration in manufacturing in line with the concept of "Industry 4.0" (Lasi et al. 2014; Ghobakhloo 2020).

Example usage

Both `piblin` and `hermes-rheo` are in the Python Package Index (PyPI) and can be quickly installed using `pip`:

```
pip install piblin
pip install hermes-rheo
```

The tutorial notebooks folder in the `hermes-rheo` code repository contains multiple examples that showcase the software's functionality in detail (Perego 2024c). These tutorials demonstrate the practical steps required for the Python package to be used to carry out the analyses described herein. In addition, the software documentation, including automati-

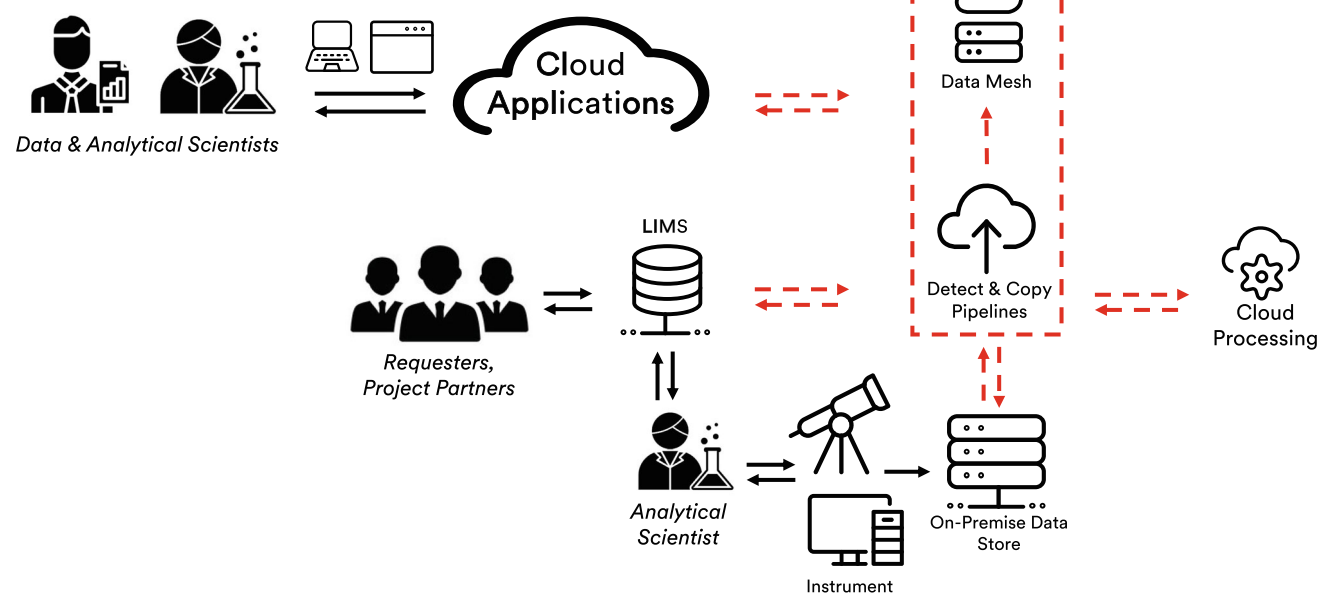


Fig. 1 Schematic representation of a cloud-based system for highly automated rheological data analysis and reporting. Data and metadata flow through the system into structured databases, and results are made

available to scientists via cloud applications, as well as to internal and external partners through a Laboratory Information Management System (LIMS)

ically generated API docs, can be found at Perego (2024b). This documentation provides in-depth details on how the Python package works and allows the provided analyses to be integrated with broader automated workflows, including cloud-based analysis applications.

Results and discussion

Validation of OWCh vs traditional methods

To validate the OWCh methodology, a test protocol was designed to measure the viscoelastic response of an acrylic adhesive sample at 25°C using three distinct approaches: a discrete frequency sweep, an OWCh experiment, and a multi-wave frequency superposition method. Five replicate tests were performed, each with a new sample, and the resulting data were processed using the `piblin` and `hermes-rheo` packages. Figure 2 presents the average results from these replicates, revealing excellent agreement among all three techniques and confirming the robustness of the OWCh approach for viscoelastic characterization.

Accelerated time–temperature superposition

Time–temperature Superposition (tTS) is a foundational technique for characterizing the viscoelastic behavior of materials over broad frequency and temperature ranges, thereby informing predictions of long-term and high-frequency mechanical performance. Traditionally, tTS experiments employ a series of discrete frequency sweeps at multiple isothermal conditions, yielding a family of self-similar curves for the datasets $\{G'(\omega_i, T_j), G''(\omega_i, T_j)\}$. These curves are collapsed onto a master curve by selecting a reference temperature T_r and shifting along the frequency axis to reduced coordinates (G'_r, G''_r, ω_r) , where $G'_r = b_T G'$, $G''_r = b_T G''$ and $\omega_r = a_T \omega$. The fidelity of this shift protocol is typically assessed by comparing the horizontal shift factors a_T with a suitable model (e.g., the Williams–Landel–Ferry equation) (Ferry 1980). For this study, we set the vertical shift factors, b_T , to unity. This choice simplifies direct comparisons between superposition performed using different techniques and reflects our observation for this adhesive that horizontal shifting alone suffices to collapse all viscoelastic properties of interest—namely G' , G'' ,

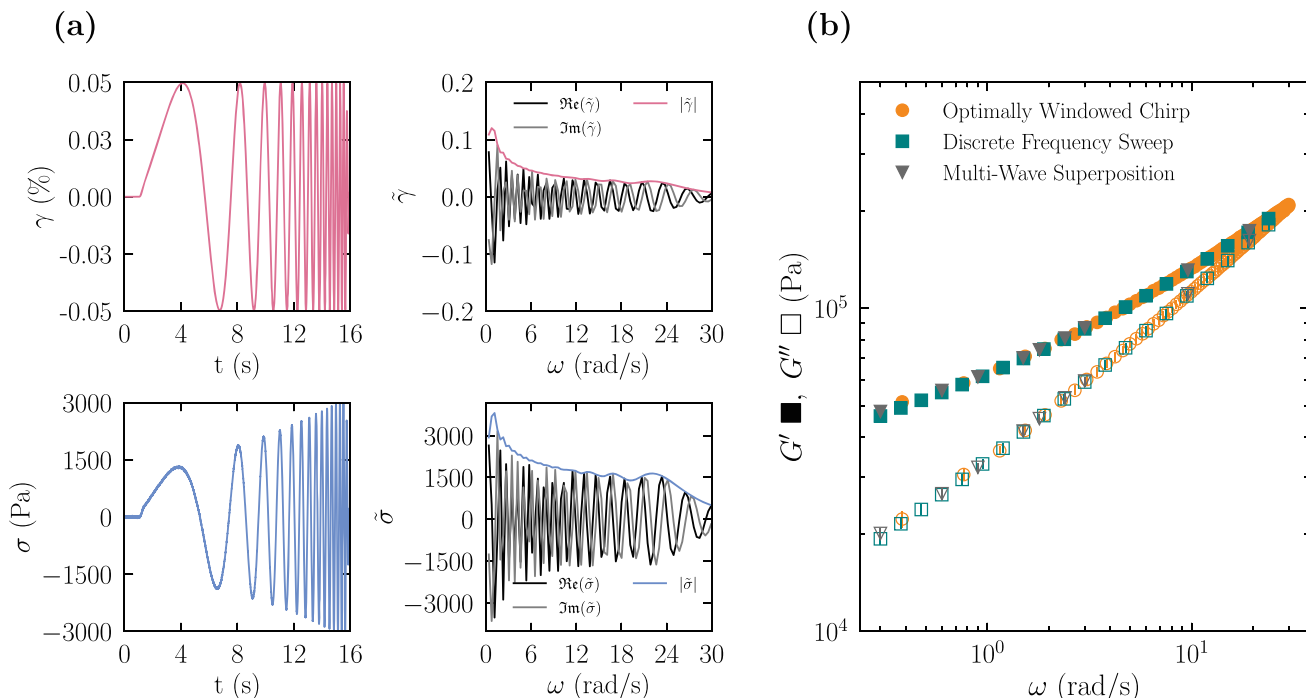


Fig. 2 **a** Top left: Input OWCh strain signal, $\gamma(t)$, as a function of time with wave parameters $r = 0.1$, $\omega_1 = 0.3 \text{ rad/s}$, $\omega_2 = 30 \text{ rad/s}$, $\gamma_0 = 5\%$, $t_w = 1 \text{ s}$, and $T_{owc} = 14 \text{ s}$. Top right: Real, imaginary, and absolute values of the transformed strain signal $\tilde{\gamma}$ in the Fourier domain (see Eq. 2), plotted against frequency. In the Fourier domain, the real component represents the in-phase (elastic) response and the imaginary component the out-of-phase (viscous) response. Bottom left: Measured output shear stress σ as a function of time. Bottom right: Real, imaginary,

and absolute values of the transformed stress signal $\tilde{\sigma}$ in the Fourier domain, also plotted against frequency. **b** Comparison of the storage (filled markers) and loss (empty markers) moduli as a function of frequency for the high strength acrylic adhesive at $T = 25^\circ\text{C}$, collected using discrete frequency sweep, multi-wave superposition, and OWCh methods. The data represent the average of five repeats, with error bars smaller than the symbol size. Excellent agreement is observed between the OWCh technique and the more established methods

and $\tan \delta$. Because $\tan \delta(\omega_i, T_j) = G''(\omega_i, T_j)/G'(\omega_i, T_j)$, the loss tangent is inherently invariant under vertical scaling, and empirically, we find $b_T \approx 1$ over the investigated temperature range.

Although the discrete frequency approach provides high spectral resolution, its data acquisition times—from a few minutes to half an hour per temperature—pose a significant throughput constraint, especially for materials requiring extensive thermal characterization. In this section, we assess the utility of an OWCh-based tTS workflow relative to conventional frequency sweeps. By replacing multiple discrete-sweep experiments with a single, frequency-modulated signal at each temperature, OWCh reduces the data collection time by an order of magnitude or more. However, successful implementation requires judicious selection of the strain/stress amplitude to preserve linear viscoelastic conditions at all thermal states. A recommended best practice entails conducting preliminary OWCh trials at the thermal extremes to establish bounds for the input signal amplitude. Interpolation of these amplitude values may suffice for intermediate temperatures, although refined adjustments could be necessary near major transition events such as the glass transition temperature or for rapidly mutating systems.

Despite the extra calibration steps, OWCh tTS protocols can markedly accelerate the generation of master curves without compromising accuracy. Iterative fine-tuning of parameters—such as transducer range or the number of consecutive OWCh cycles—may be warranted for complex

rheological profiles, yet this additional overhead remains minimal compared to the time consumed by discrete sweeps. In essence, OWCh-driven tTS methodologies offer both the spectral breadth of traditional tTS and the time-saving advantages of simultaneous multi-frequency excitation, thereby expanding the scope of high-throughput rheological characterization.

In principle, the OWCh technique is sufficiently flexible to be applied across various rheometers, geometries, and deformation modes, making it a viable alternative to DFS for large-scale dataset generation (e.g., tTS master curves). Although Sheridan et al. employed a different frequency-modulated input in a DMA (dynamic mechanical analysis) context, their findings align with our demonstration of high-throughput viscoelastic measurements using OWCh (Sheridan et al. 2024). Here, we compare an OWCh-based tTS protocol against master curves obtained from DFS using a thermorheologically simple pressure-sensitive adhesive (PSA) material (3M™ High-Strength Acrylic Adhesive 300LSE).

To validate the OWCh tTS protocol against traditional frequency sweeps, we first compared the two methods over the same temperature range, from -40 to 150°C , in 10°C increments (Fig. 3). Overall, OWCh data show good agreement with discrete frequency sweep (DFS) measurements, reflecting the versatility of the modulated approach. However, as the temperature drops below the glass transition temperature ($T_g \approx 0^\circ\text{C}$), deviations become increasingly apparent. In

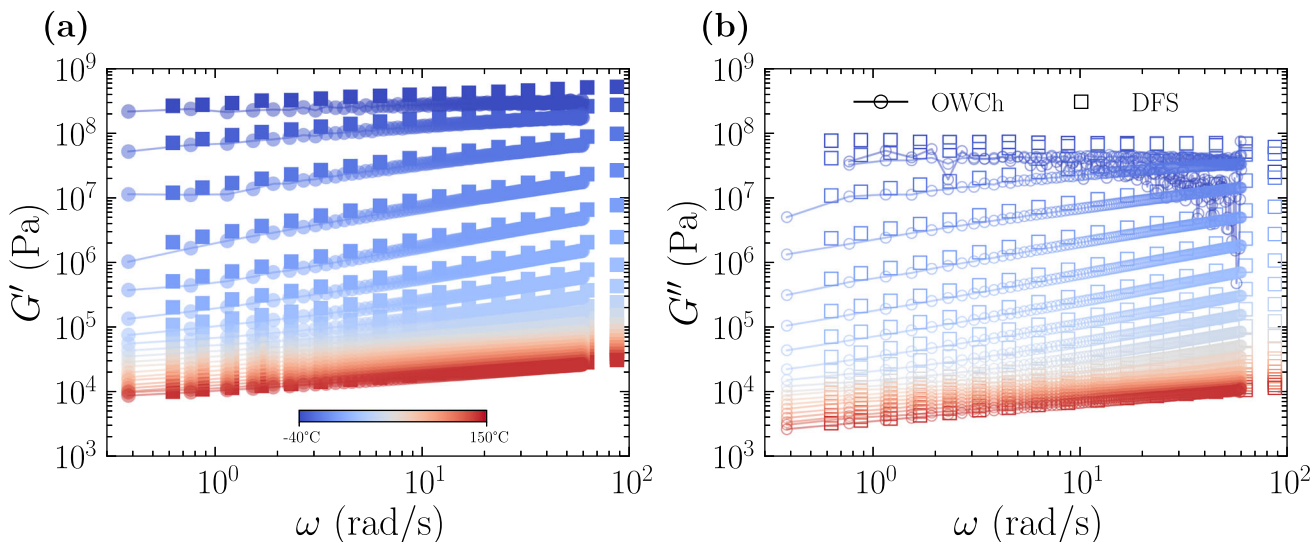


Fig. 3 Comparison of the storage modulus (a) and loss modulus (b) measured using discrete frequency sweep and OWCh (filled and hollow markers respectively) at various temperatures, from $T = -40^\circ\text{C}$ (blue) to $T = 150^\circ\text{C}$ (red), using 10°C increments. For both methods, the equilibration time between isothermal steps was set at 180 s. The discrete frequency sweep conditions corresponded to 15 logarithmically

spaced points between $\omega_1 = 0.6 \text{ rad/s}$ and $\omega_2 = 125 \text{ rad/s}$ with $\gamma_0 = 1\%$, and the instrument control loop was used with a 50% adjustment between $0.01\% \leq \gamma \leq 5\%$ for $1 \text{ g cm} \leq T \leq 10 \text{ g cm}$. For OWCh, the conditions were $\omega_1 = 0.3 \text{ rad/s}$ and $\omega_2 = 60 \text{ rad/s}$ with $\gamma_0 = 1\%$, over a duration of 15 s at each temperature ($T_{owc} = 14 \text{ s}$ and $t_w = 1 \text{ s}$)

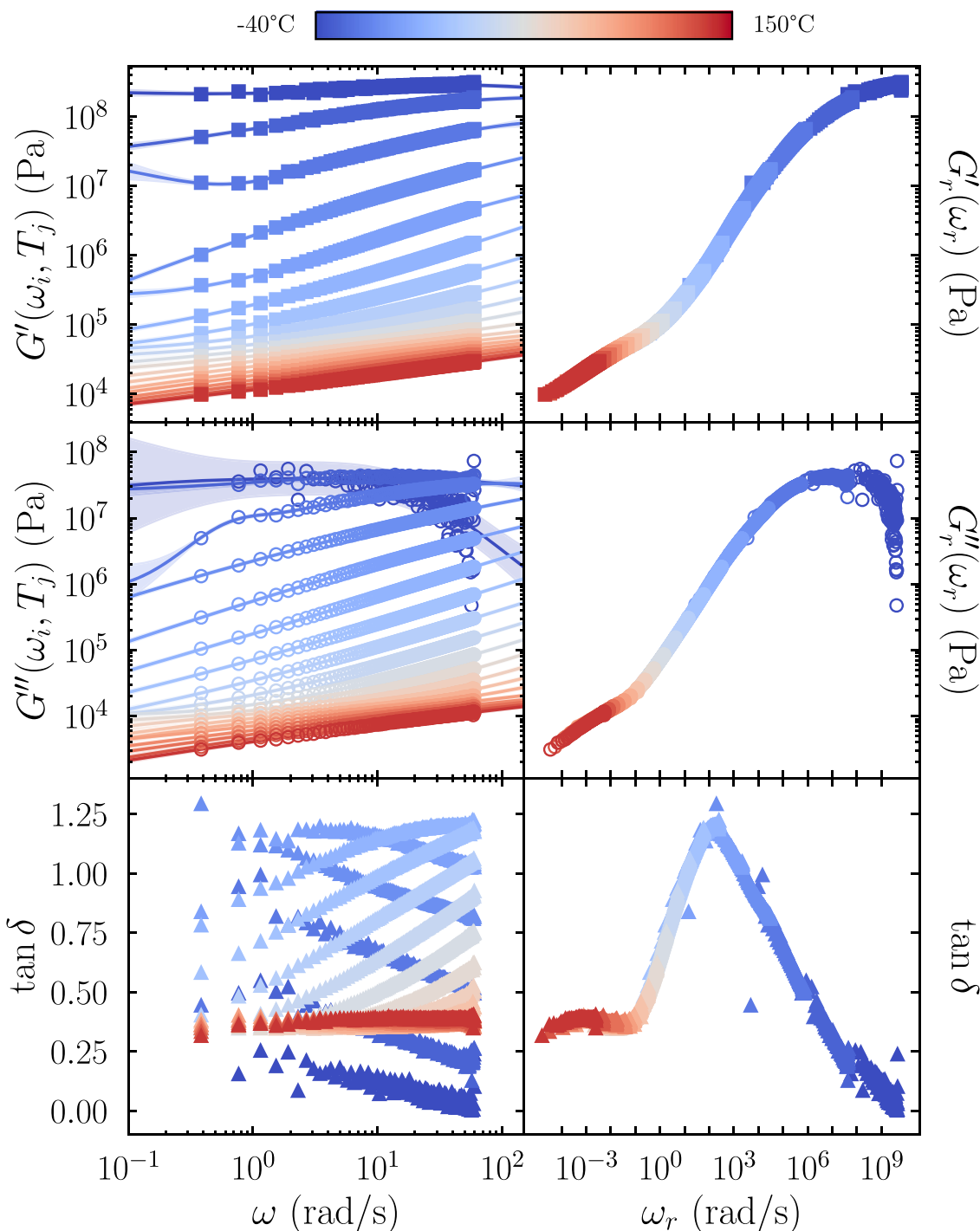


Fig. 4 Storage and loss modulus data, as well as phase-angle measurements, collected via OWCh from $T = -40^\circ\text{C}$ to $T = 150^\circ\text{C}$ in 10°C increments. The solid lines and shaded regions represent the posterior mean, $m(t)$, and its corresponding uncertainty bounds, $m(t) \pm s(t)$,

obtained from Gaussian process regression. The time-temperature superposition (tTS) master curves (right) were automatically constructed via horizontal shifting using maximum *a posteriori* estimation, with a reference temperature $T_r = 20^\circ\text{C}$

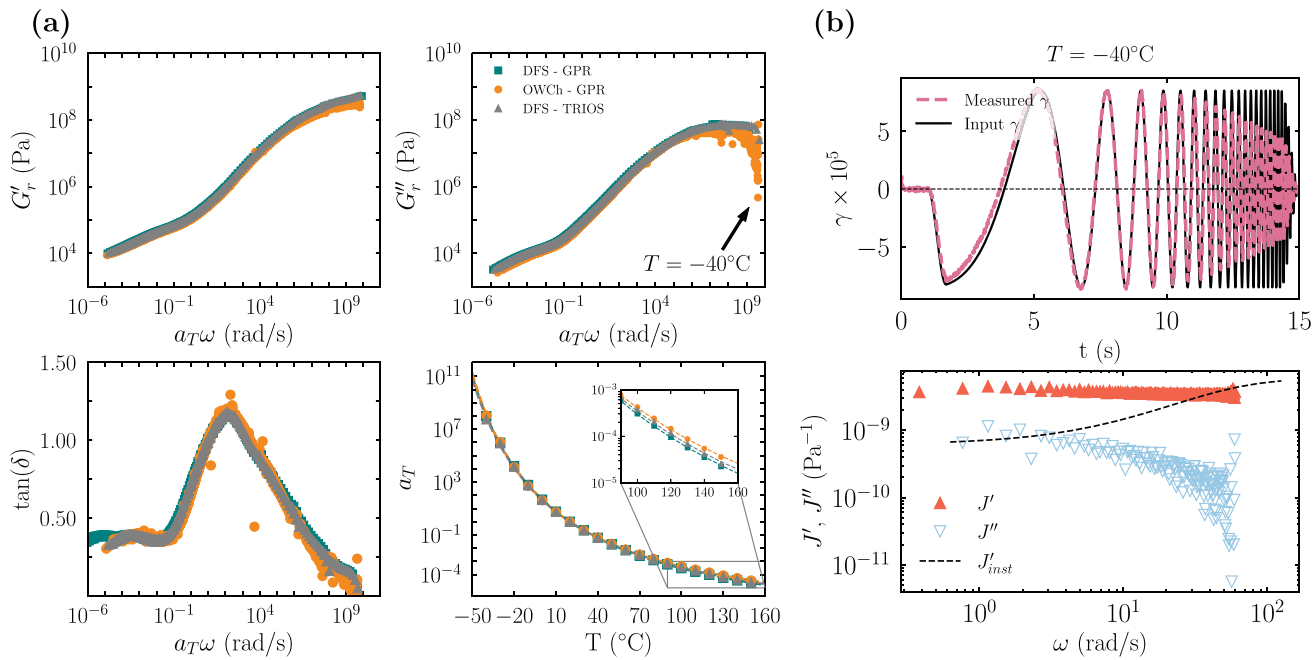


Fig. 5 **a** Comparison of time–temperature superposition (tTS) master curves obtained via OWCh and discrete frequency sweeps (DFS), using an automated data-driven superposition approach. For the DFS data, a separate master curve was also generated using TRIOS software. Bottom-right plot shows the horizontal shift factors a_T as a function of temperature for all three methods (OWCh-GPR, DFS-GPR, DFS-

TRIOS). **b** Top: Comparison of the user-programmed OWCh strain input and the strain measured by the rheometer’s transducer at -40°C . The transducer could not fully replicate the input signal under these conditions, leading to systematic error in G'' . Bottom: Storage (J') and loss (J'') compliance obtained via OWCh at -40°C (below T_g) together with the instrument compliance (J'_{inst})

particular, at -40°C , the OWCh signal exhibits higher noise levels especially at the highest frequencies. The underlying causes for this are discussed later in the text.

Despite these small low-temperature discrepancies, the OWCh-based time–temperature superposition (tTS) analysis remains robust. Using the `AutomatedMastercurve` transform in `hermes-rheo`—which uses the master-curve algorithms developed by Lennon et al. (2023)—we generated master curves for G' , G'' , and $\tan(\delta)$ via Gaussian process regression with maximum *a posteriori* estimation. As illustrated in Fig. 4, the datasets for all temperatures collapse effectively onto single master curves, even incorporating the noisier data at -40°C . This outcome demonstrates both the resilience of the data-driven superposition approach to elevated levels of signal noise (Lennon et al. 2023) and the practical efficiency of OWCh for high-throughput rheological measurements.

In Fig. 5a, we compare time–temperature superposition (tTS) master curves obtained from OWCh and discrete frequency sweeps (DFS), with both methods employing an automated, data-driven superposition approach. For the DFS data, an independent master curve was additionally constructed using TA Instruments’ TRIOS software to provide a second reference for comparison. The close overlap of the resulting master curves, along with the nearly identical val-

ues of the computed horizontal shift factors a_T , demonstrates strong agreement among the OWCh-GPR, DFS-GPR, and DFS-TRIOS analyses, thereby validating OWCh as an effective alternative to a series of discrete frequency sweeps.

The lines passing through the data represent the best fit to the Williams–Landel–Ferry (WLF) equation (Ferry 1980):

$$\log_{10}(a_T) = -\frac{C_1(T - T_r)}{C_2 + (T - T_r)}, \quad (12)$$

where T_r denotes the reference temperature and C_1 and C_2 are material-specific empirical constants. In our analysis, we set $T_r = 20^\circ\text{C}$; Table 1 summarizes the WLF parameters obtained for the three datasets.

As noted by the inset arrow shown in the upper right plot of Fig. 5a, at $T = -40^\circ\text{C}$ the loss modulus G'' exhibits considerable high-frequency noise. To identify its origin, we compared the user-programmed OWCh strain input with the

Table 1 WLF fit parameters for different tTS methods

Method	C_1	$C_2 (\text{ }^\circ\text{C})$
DFS-GPR	9.19	128
OWCh-GPR	8.63	124
DFS-TRIOS	9.04	129

strain recorded by the rheometer's transducer at the same temperature (top panel of Fig. 5b). The comparison reveals a sudden drop in strain amplitude immediately before the Tukey window onset, indicating that the instrument is nearing its torsional compliance or acceleration limits. This behavior is consistent with the upper-threshold compliance effects recently reported by Hossain et al. (2025) for high-stiffness, high-frequency regimes.

To verify quantitatively that the origin of the noise arises from instrument limitations, we adopted Hossain's recommendation to work in compliance space, transforming the dynamic moduli to dynamic compliances via $J' = G'/(G'^2 + G''^2)$ and $J'' = G''/(G'^2 + G''^2)$ (Ferry 1980) (plotted in the bottom panel of Fig. 5b), and computing the torsional compliance threshold of the instrument as follows:

$$J'_{\text{inst}}(\omega) = \frac{1}{K_\theta(\omega)} \frac{C_\gamma}{C_\sigma}, \quad (13)$$

where $C_\gamma = 4.37 \text{ rad}^{-1}$ and $C_\sigma = 9947183 \text{ Pa/N}\cdot\text{m}$ are, respectively, the strain and stress conversion coefficients obtained from the instrument software and where $K_\theta(\omega)$ is the frequency dependent torsional stiffness of the total system defined as follows: $1/K_\theta(\omega) = 1/K_{\theta,\text{PP}} + 1/K_{\theta,\text{trans}}(\omega)$ where $K_{\theta,\text{PP}}$ and $K_{\theta,\text{trans}}(\omega)$ represent the geometry and transducer stiffness, respectively. For our 8-mm stainless steel parallel plates, $1/K_{\theta,\text{PP}} = 0.705 \text{ mrad/N}\cdot\text{m}$. The transducer stiffness $K_{\theta,\text{trans}}(\omega)$ is not reported when using the arbitrary wave method in TRIOS; therefore, we approximate $K_{\theta,\text{trans}}(\omega)$ with transducer stiffness reported by the software during the discrete frequency sweeps experiment. This yields values of J'_{inst} rising from $6.7 \times 10^{-10} \text{ Pa}^{-1}$ at 0.6 rad/s to $5 \times 10^{-9} \text{ Pa}^{-1}$ at 60 rad/s (black dashed line, bottom panel of Fig. 5b). When operating near these thresholds, compliance corrections become essential to maintain data integrity. Because the OWCh protocol probes a broad frequency spectrum in a single run, the effective upper limit of the measurable compliance for reliable strain control can be lower than in discrete frequency tests. Consequently, although OWCh accelerates data acquisition, mechanical limitations at low temperatures and high frequencies may introduce additional noise when the material modulus exceeds the torsional compliance of the instrument.

Although our compliance analysis was based on values explicitly extracted from discrete frequency sweep experiments, it is worth noting that TRIOS includes internal compliance correction protocols for both transducer and fixture deformation, based on servo-driven angular displacement feedback. These corrections are automatically applied during standard oscillatory tests and help reduce compliance-related artifacts in linear viscoelastic measurements (Franck 2006). However, such real-time corrections are not currently

available when using arbitrary waveform protocols, making direct estimation and correction of compliance effects essential for accurate interpretation of high-frequency OWCh data.

In summary, the OWCh-based tTS protocol delivers master curves comparable to those obtained via conventional discrete frequency sweeps, while achieving markedly higher data density and reduced acquisition time. In our study, the OWCh approach produced approximately 1300 data points across the master curve—about 4.5 times more than the roughly 290 points typically obtained with standard discrete tTS sweeps (using seven points per decade). Moreover, the overall acquisition time was reduced from 90 to 53 min (including 3 min of equilibration time at each temperature), representing a 40% improvement in speed. These enhancements underscore the potential of OWCh for rapid, high-resolution rheological characterization.

OWCh on mutating materials

A key motivation for developing time-resolved mechanical spectroscopy via OWCh is the need to characterize so-called mutating materials (e.g., gels, thermosets), whose characteristic timescales for structural evolution can be shorter than the total duration of a discrete frequency sweep (Mours and Winter 1994). These materials constitute a substantial portion of 3MTM's product portfolio, making rapid and accurate rheological characterization essential for establishing structure–property relationships that guide material design and corresponding processing protocols.

To demonstrate the effectiveness of OWCh in this context, we examined a UV-curable acrylate system undergoing *in situ* crosslinking. Over approximately 750 s of total reaction time, we applied 70 consecutive OWCh signals, each lasting 7 s (with an addition waiting time of 3 s). A video illustrating the concurrent evolution of strain, stress, and viscoelastic moduli (both in the time and frequency domains) is provided in the Supplementary Information. Figure 6a shows the temporal evolution of the frequency-dependent complex modulus $|G^*(\omega_i, t_j)|$ from the uncured state at $t = 0 \text{ s}$ (yellow markers) to a final highly crosslinked state at $t = 763 \text{ s}$ (violet markers).

Following a similar approach to tTS, we implemented an automated data-driven superposition of the measured complex modulus data by using each OWCh wave's start time as the state variable instead of temperature. We refer to this procedure as time-curing superposition (tCS). As with tTS, a reference state must be defined; here, we select the initial time ($t_0 = 0 \text{ s}$) as the reference age and shift all subsequent data onto this reference. Vertical shift factors b_t were set to unity.

As depicted in Fig. 6b, the $|G^*|$ data collapse into a well-defined master curve, indicating that the underlying material changes can be captured effectively using only horizontal

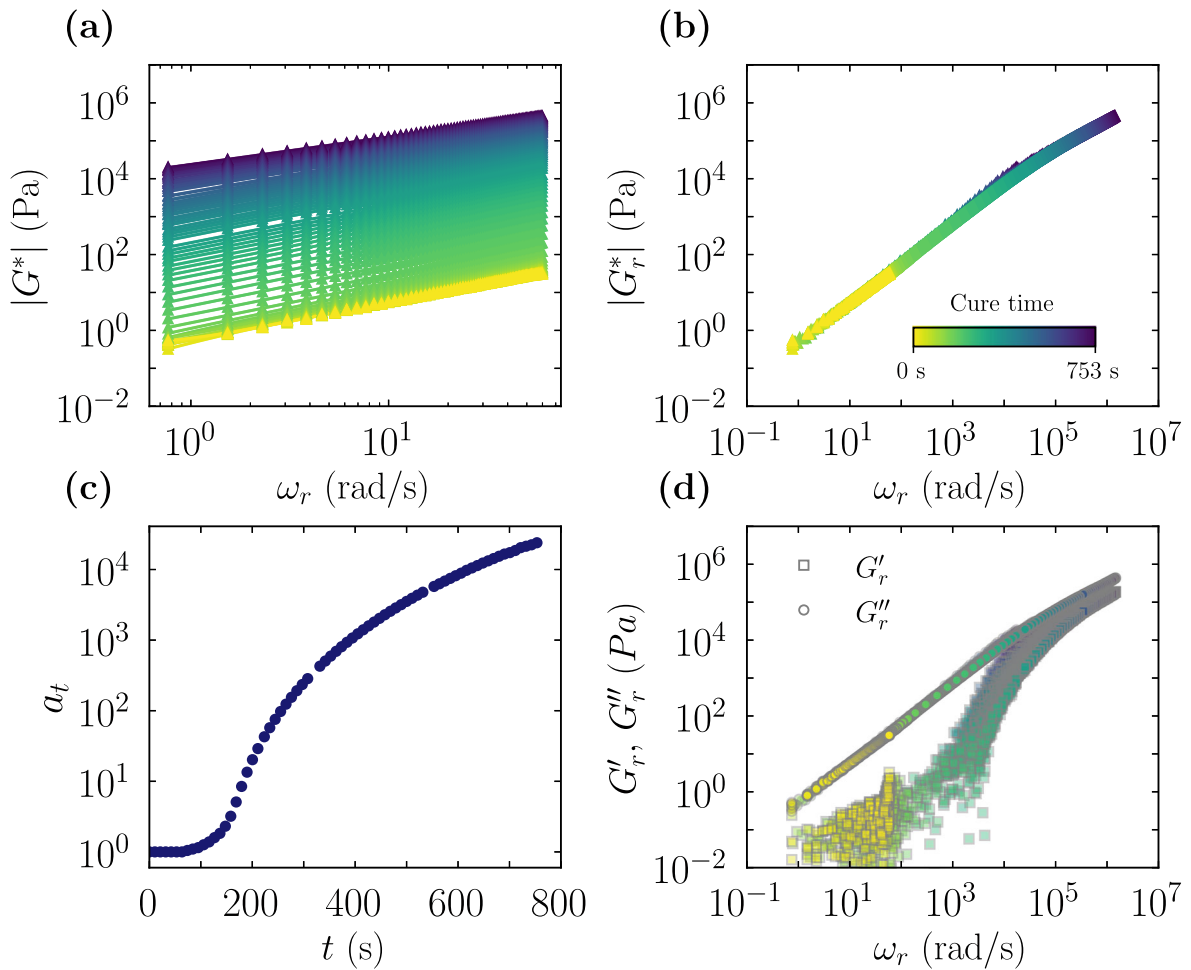


Fig. 6 Absolute value of the complex modulus, $|G^*|$, as a function of frequency for a UV-curable acrylate, tracked over 70 OWCh waves from $t = 0$ s (uncured; yellow markers) to $t = 763$ s (highly crosslinked; violet markers). The solid lines and shaded regions show the posterior mean $m(t)$ and its uncertainty bounds, $m(t) \pm s(t)$, estimated via Gaussian process regression. **a** Master-curve superposition of $|G^*(\omega_i, t_j)|$ at various

curing times. **b** The horizontal shift factors, a_t , used to construct the $|G_r^*|$ master curve. **c** Master curve for the reduced storage modulus (G'_r , squares) and loss modulus (G''_r , circles) constructed using the horizontal shift factors determined in **c**. These data were collected using an OWCh waveform with $\omega_1 = 0.6$ rad/s, $\omega_2 = 60$ rad/s, $T_{owc} = 7$ s, and $r = 0.1$, giving a time–bandwidth product $TB = 66$

shifting. The corresponding age-dependent shift factors, a_t , are shown in Fig. 6c. By applying these same shifts to the individual curves of storage (G') and loss (G'') moduli at each material age time, we obtained the master curves shown in Fig. 6d. Early in the cure (short reaction times), the measurements of G' show high levels of noise due to the predominantly viscous nature of the initial material; once crosslinking proceeds, the elastic contribution increases significantly.

Notably, relying on the magnitude of the complex modulus $|G^*| = \sqrt{(G')^2 + (G'')^2}$ to determine shift factors is especially advantageous here, because $|G^*|$ incorporates both the elastic and viscous components of the viscoelastic response. Consequently, even when the contributions of G' are initially

negligible, the combined information in $|G^*|$ still provides a robust dataset for superposition. Overall, these results confirm that OWCh can deliver high-density, time-resolved data for rapidly mutating systems, overcoming the temporal constraints inherent to discrete frequency sweeps.

To further quantify the curing process, we compute the magnitude of the complex viscosity, $|\eta^*|$, using its formal definition:

$$|\eta_r^*| = \frac{|G_r^*|}{\omega_r} = \frac{\sqrt{(G'_r)^2 + (G''_r)^2}}{\omega_r}. \quad (14)$$

The complex viscosity is a key parameter in the modeling of the cure kinetics of various 3M™ adhesive formulations used in complex and sometimes delicate assemblies. In such

situations, kinetic models of the transient complex viscosity, and in some cases the full viscoelastic spectrum, serve as indispensable tools for optimizing manufacturing and product design processes.

Figure 7a shows the resulting master curve of $|\eta^*|$, normalized by shift factors a_t and plotted as a function of ω_r . An unexpected uptick appears in the range $10^2 \lesssim \omega_r \lesssim 1.5 \times 10^4$ rad/s, suggesting that the rate of material transformation during early curing exceeds the measurement timescale.

To investigate this phenomenon, we computed the mutation number Mu by tracking the evolution of a representative viscoelastic metric g (taken here to be $|G^*|$) across consecutive OWCh tests:

$$Mu(t_i, \omega_j) \approx \frac{T_{\text{owc}} \ln\left(\frac{g(t_i, \omega_j)}{g(t_{i-1}, \omega_{j-1})}\right)}{t_i - t_{i-1}}, \quad (15)$$

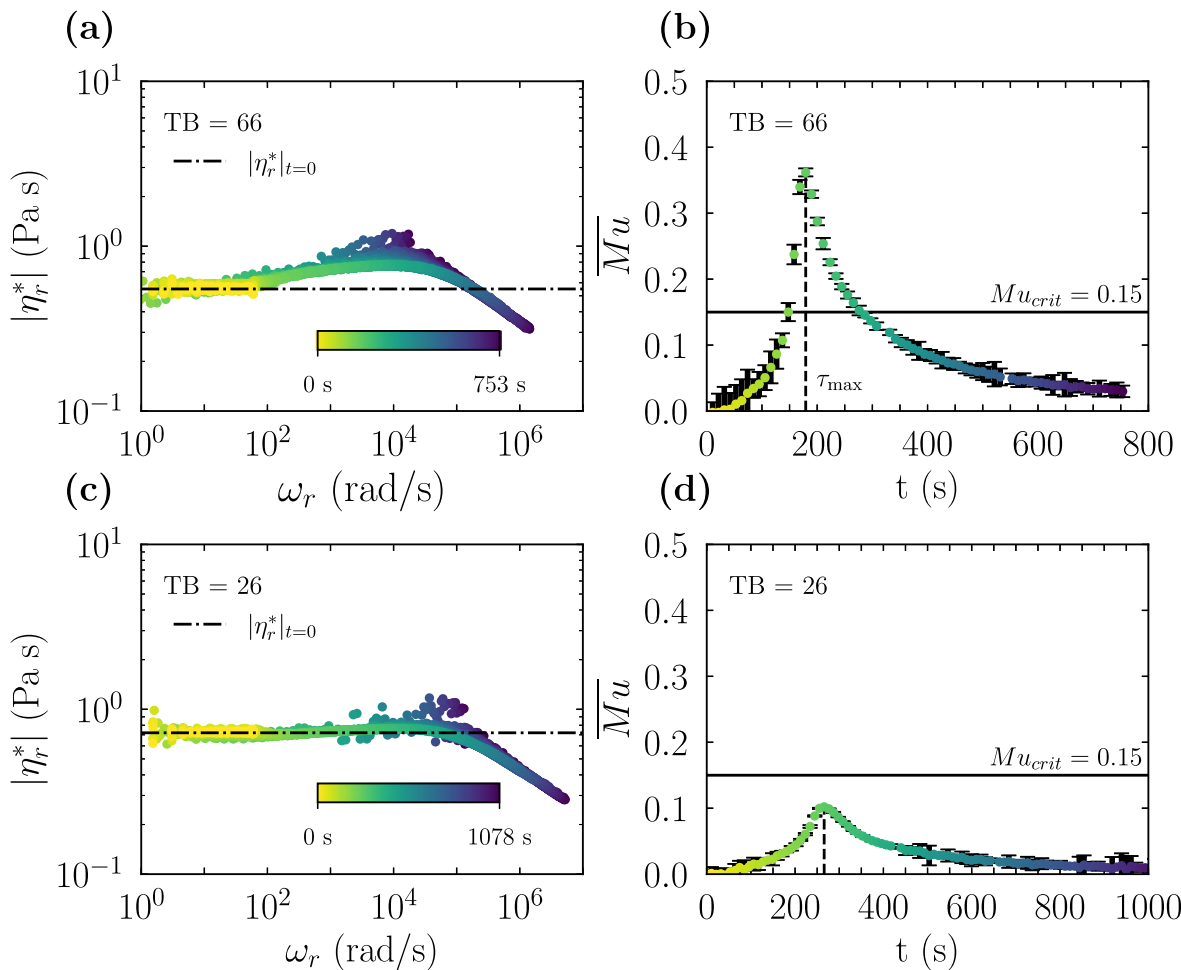


Fig. 7 **a** Master curve of the complex viscosity, $|\eta^*|$, normalized by a_t and plotted against reduced frequency ω_r . The artificial uptick occurs within the frequency range $10^2 \lesssim \omega_r \lesssim 1.5 \times 10^4$ rad/s. **b** Time evolution of the frequency-averaged mutation number, $Mu(t)$ computed

where i indexes the time of the i^{th} OWCh wave, j indexes the measured frequency, and $t_i - t_{i-1}$ is the time interval between successive OWChs.

Figure 7b displays the frequency-averaged value of the mutation numbers $\overline{Mu} = Mu(t_i, \overline{\omega_j})$, which exhibits a pronounced rise beginning around 150 s, followed by a gradual decline. This onset of a rapid increase in \overline{Mu} correlates with the sudden increase in the horizontal shift factors, as shown in Fig. 6c, and corresponds to the rapid crosslinking phase during initial curing. During this phase, the viscoelastic response of the acrylate increases sharply as the material cures, after which chain mobility decreases and the kinetics slow down.

To mitigate this artifact that is revealed by examining the evolution in the reduced complex viscosity $|\eta_r^*(\omega_i, t_j)|$, we increased the minimum angular frequency ω_1 in the OWCh to shorten the measurement duration T_{owc} and thereby con-

using Eq. 15 with $g = |G^*|$. **c** Complex viscosity results after setting $\omega_1 = 1.5$ rad/s, which lowers the time-bandwidth product to $TB = 26$ and keeps $Mu < 0.15$. **d** Corresponding plot of $\overline{Mu}(t)$ vs. cure time for the experiment at $TB = 26$

strain the mutation number Mu below the critical threshold, $Mu \leq Mu_{\text{crit}}$, where the critical threshold is set to $Mu_{\text{crit}} = 0.15$, as recommended by Rathinaraj et al. (2022). However, this adjustment has the concomitant effect of reducing the time–bandwidth product (TB) below the recommended level for optimal spectral resolution (Geri et al. 2018). This trade-off underscores the challenge of capturing rapid rheological transitions while maintaining high-frequency resolution in rapidly mutating systems.

An approximate guideline for selecting the preferred range of initial test frequency ω_1 is provided by

$$\omega_1 > \frac{4\pi}{3 Mu_{\text{crit}} \tau_{\max}}, \quad (16)$$

where τ_{\max} is the characteristic time at $\max(\overline{Mu})$. By setting $\omega_1 = 1.5 \text{ rad/s}$, $\omega_2 = 60 \text{ rad/s}$, $T_{\text{owc}} = 2.8 \text{ s}$, and $r = 0.1$, we reduced the time bandwidth from $TB = 66$ to $TB = 26$. As shown in Fig. 7c and d, under these revised conditions, the frequency-averaged mutation number for each OWCh, \overline{Mu} , remains below Mu_{crit} for the entire experiment, thereby eliminating the artificial uptick in $|\eta_r^*|$. This example demonstrates that monitoring the rate of sample mutation and careful selection of ω_1 are essential when studying rapidly mutating materials to minimize measurement artifacts.

In addition to eliminating the artificial uptick in complex viscosity, our analysis revealed a subtle but important insight. Although the original time–cure superposition master curve (Fig. 6) obtained from an OWCh with $TB = 66$ appeared to collapse satisfactorily at first glance, the computed values of complex viscosity exhibited a significant artifact during the early curing phase. This discrepancy suggests that, despite the high data density provided by OWCh, visual agreement of the master curve superposition alone may mask underlying issues that arise from the material’s rapid transformation kinetics. By calculating and plotting the complex viscosity, we are able to scale out the leading-order linear frequency dependence ($|G_r^*| \propto \omega_r$) thus exposing the more nuanced frequency-dependent features of the sample viscoelasticity resulting from the cure kinetics. This “masking” effect of linear frequency scaling was highlighted by Plazek in his 1995 Bingham Medal Address (Plazek 2024). Therefore, it is essential to compute the mutation number for each chirp so to ensure that $\overline{Mu} \leq Mu_{\text{crit}}$ throughout the duration of the experiment (Winter and Chambon 1986) and adjust the OWCh waveform parameters accordingly. The complex moduli, together with the master curves for storage and loss modulus and the shift factors for the experiment conducted using an OWCh with $TB = 26$ (Fig. 7c and d), are provided in the Supplementary Information.

Conclusions

In this work, we have demonstrated that the OWCh methodology offers a robust, high-throughput alternative to conventional discrete frequency sweeps (DFS) for rheological characterization of both reversibly and irreversibly mutating materials. It thus allows more rapid and robust computation of master curves relevant to time–temperature superposition (tTS) and time–curing superposition (tCS). By carefully selecting waveform parameters that respect rheometer hardware limitations and material-specific linear viscoelastic constraints, OWCh can be readily adapted to a range of instruments and test geometries. Moreover, the seamless integration of high-volume data analysis—through packages such as `piblin` and `hermes-rheo`—enables efficient processing, visualization, and interpretation of chirp-based tests.

Compared to DFS, OWCh significantly accelerates the collection of master curve data, providing both higher data density and broader frequency coverage in considerably less time. This advantage is particularly evident in tTs protocols, where OWCh allows for faster and more comprehensive data acquisition. Additionally, we have shown that the methodology is well suited to capturing transient behavior in mutating materials, enabling frequency-resolved kinetic insights during curing or gelation processes. This capacity to build time–cure superposition master curves has important implications for the modeling of cure kinetics and the design of materials with tunable properties.

Although OWCh has been successfully implemented under various testing conditions, several opportunities remain for further method refinement and expansion. For instance, performing OWCh experiments under continuous temperature-sweep protocols (rather than at a sequence of isothermal test states) could provide insights into dynamically evolving non-equilibrium material states. Combining OWCh waveforms with other simultaneous microstructural characterization protocols (e.g., Rheo-IR, Rheo-Raman) might help elucidate structure–property relationships in real time. Extending OWCh beyond shear deformation—to extensional or torsional modes—would also broaden the technique’s applicability, particularly for soft solids, adhesives, and composites that experience complex multi-axial loading in industrial settings.

Finally, collaborative development with instrument manufacturers is vital to optimize software control loops and identify hardware parameters that can fully exploit the potential of OWCh. Enhancements such as automated bias correction, real-time adjustments of the forcing amplitude (either imposed strain or imposed stress) to overcome instrument compliance limits, or built-in data-driven superposition routines would streamline the technique, reducing manual

intervention and ensuring reproducible, high-fidelity measurements. Taken together, these developments outline a clear path toward a more integrated, versatile, and efficient rheometric infrastructure capable of meeting the needs of data-science techniques and the growing demands of modern material development and process optimization.

Supplementary Information

Supporting data are available in the Supplementary Information online, including: animation of the evolution in the storage modulus G' and loss modulus G'' evolution with frequency, alongside strain input $\gamma(t)$ and stress output $\sigma(t)$, for a UV-curable acrylate during crosslinking (Video S1); magnitude of complex modulus $|G_r^*|$, storage modulus G'_r , and loss modulus G''_r with Time-Cure Superposition master curves for the OWCh experiment at $T_B = 26$ (Figure S1).

Supplementary Information The online version contains supplementary material available at <https://doi.org/10.1007/s00397-025-01511-0>.

Acknowledgements The authors express their gratitude to Ross Behling (3M™) for providing the samples used for this study and offering valuable support, Emily Ma (3M™) and Amanda Leone (3M™) for their contributions to the selection and preparation of UV-curing materials and insightful discussions on cure kinetics, and Mark McCormick (3M™) for valuable discussions regarding fast Fourier transform (FFT) analysis.

Materials Availability 3M™ High-Strength Acrylic Adhesive 300LSE is commercially available and can be obtained from 3M™ or authorized distributors.

Code Availability The piblin and hermes-rheo packages are released under the MIT Open Source License and available via PyPI. Source code can be found at <https://github.com/3mcloud/piblin> and <https://github.com/3mcloud/hermes-rheo>.

References

- 3M: 3M Adhesive 300LSE Technical Data Sheet. <https://multimedia.3m.com/mws/media/2366131O/3M-Adhesive-Transfer-Tape-9472LE.pdf?pif=000044?locale=en-US>
- Athanasiou T, Geri M, Roose P, McKinley GH, Petekidis G (2024) High-frequency optimally windowed chirp rheometry for rapidly evolving viscoelastic materials: application to a crosslinking thermoset. *J. Rheol.* 68(3), 445–462. <https://doi.org/10.1122/8.00007937>
- Au WW, Simmons JA (2007) Echolocation in dolphins and bats. *Phys. Today* 60(9):40–45. <https://doi.org/10.1063/1.2784683>
- Bouzid M, Keshavarz B, Geri M, Divoux T, Del Gado E, McKinley GH (2018) Computing the linear viscoelastic properties of soft gels using an optimally windowed chirp protocol. *J. Rheol.* 62(4):1037–1050. <https://doi.org/10.1122/1.5024066>
- Curtis DJ, Holder A, Badiee N, Claypole J, Walters M, Thomas B, Barrow M, Deganello D, Brown MR, Williams PR, Hawkins K (2015) Validation of optimal Fourier rheometry for rapidly gelling materials and its application in the study of collagen gelation. *J. Non-Newtonian Fluid Mech* 222:253–259. <https://doi.org/10.1016/j.jnnfm.2015.01.003>. Rheometry (and General Rheology): Festschrift dedicated to Professor K Walters FRS on the occasion of his 80th birthday
- Chen DT, Wen Q, Janmey PA, Crocker JC, Yodh AG (2010) Rheology of soft materials. *Annu Rev Condens Matter Phys* 1(1):301–322. <https://doi.org/10.1146/annrev-conmatphys-070909-104120>
- Dow: Voranol 220260 Technical Data Sheet. <https://www.dow.com/en-us/document-viewer.html?docPath=/content/dam/dcc/documents/400/400-001/400-00101240en-voranol-220260-tds.pdf>
- Ferry JD (1980) Viscoelastic properties of polymers, 3rd edn. Wiley, New York
- Franck AJ (2006) Understanding instrument compliance correction in oscillation. Technical Report APN013e, TA Instruments. Technical Application Note. https://www.tainstruments.com/pdf/literature/APN013_V1_Understanding_Instrument_Compliance.pdf
- Ghobakhloo M (2020) Industry 4.0, digitization, and opportunities for sustainability. *J. Clean. Prod.* 252:119869
- Geri M, Keshavarz B, Divoux T, Clasen C, Curtis DJ, McKinley GH (2018) Timeresolved mechanical spectroscopy of soft materials via optimally windowed chirps. *Phys. Rev. X* 8:041042. <https://doi.org/10.1103/PhysRevX.8.041042>
- Ghiringhelli E, Roux D, Bleses D, Galliard H, Caton F (2012) Optimal Fourier rheometry: application to the gelation of an alginate. *Rheol. Acta* 51(5):413–420. <https://doi.org/10.1007/s00397-012-0616-z>
- Harris FJ (2005) On the use of windows for harmonic analysis with the discrete Fourier transform. *Proc. IEEE* 66(1):51–83. <https://doi.org/10.1109/PROC.1978.10837>
- Hudson-Kershaw RE, Das M, McKinley GH, Curtis DJ (2024) σ -OWCh: optimally windowed chirp rheometry using combined motor transducer/single head rheometers. *J. Non-Newtonian Fluid Mech.* 333. <https://doi.org/10.1016/j.jnnfm.2024.105307>
- Hossain MT, Macosko CW, McKinley GH, Ewoldt RH (2025) Instrument stiffness artifacts: avoiding bad data with operational limit lines of G_{max} and E_{max} . *Rheol. Acta* 64:1–13. <https://doi.org/10.1007/s00397-024-01481-9>
- Kowatsch M, Stocker H (1982) Effect of Fresnel ripples on sidelobe suppression in low time-bandwidth product linear FM pulse compression. In: IEE Proceedings F (Communications, Radar and Signal Processing), vol. 129. <https://doi.org/10.1122/1.5018715>. IET
- Landau H (1967) Sampling, data transmission, and the Nyquist rate. *Proc. IEEE* 55(10):1701–1706. <https://doi.org/10.1109/PROC.1967.5962>
- Lasi H, Fettke P, Kemper H-G, Feld T, Hoffmann M (2014) Industry 4.0. *Business & Information Systems Engineering* 6:239–242
- Lennon KR, McKinley GH, Swan JW (2023) A data-driven method for automated data superposition with applications in soft matter science. *Data-Centric Engineering* 4:13. <https://doi.org/10.1017/dce.2023.3>
- Leocmach M, Perge C, Divoux T, Manneville S (2014) Creep and fracture of a protein gel under stress. *Phys. Rev. Lett.* 113(3):038303. <https://doi.org/10.1103/PhysRevLett.113.038303>
- Mills MJL, Elmore D, Bourque A, Williams B, Patrow J, Kalstabakken K, Lotfollahi M, Perego A, Pardakhti M, Melin B, Cote B (2024) 3mcloud/piblin: Release of Initial Public Package (v0.0.0a1). Zenodo. <https://doi.org/10.5281/zenodo.13946933>
- Müller S, Massarani P (2001) Transfer-function measurement with sweeps. *Journal of The Audio Engineering Society* 49:443–471
- Madsen P, Surlykke A (2013) Functional convergence in bat and toothed whale biosonars. *Physiology* 28(5):276–283. <https://doi.org/10.1152/physiol.00008.2013>

- Mezzenga R, Schurtenberger P, Burbidge A, Michel M (2005) Understanding foods as soft materials. *Nat. Mater.* 4(10):729–740. <https://doi.org/10.1038/nmat1496>
- Mours M, Winter HH (1994) Time-resolved rheometry. *Rheol. Acta* 33:385–397. <https://doi.org/10.1007/BF00366581>
- Nussbaumer HJ (1982) The fast Fourier transform, pp. 80–111. Springer, Berlin, Heidelberg. https://doi.org/10.1007/978-3-642-81897-4_4
- Nyquist H (1928) Certain topics in telegraph transmission theory. *Trans. AIEE* 47(2):617–644. <https://doi.org/10.1109/T-AIEE.1928.5055024>
- Perego A (2024a) hermes-rheo-OWChirp design. https://github.com/3mcloud/hermes-rheo/blob/main/tutorial_notebooks/2_owchirp%20wave%20design.ipynb
- Perego A (2024b) hermes-rheo: documentation. <https://hermes-rheo.readthedocs.io/en/latest/>
- Perego A (2024c) hermes-rheo: tutorials. https://github.com/3mcloud/hermes-rheo/blob/main/tutorial_notebooks
- Plazek DJ (1996) 1995 Bingham medal address: Oh, thermorheological simplicity, wherefore art thou? *J. Rheol.* 40(6):987–1014
- Perego A, Mills MJL, Vadillo DC (2024) Hermes-Rheo (1.2.0). Zenodo. <https://doi.org/10.5281/zenodo.14453081>
- Rathinaraj JDJ, Hendricks J, McKinley GH, Clasen C (2022) Orthochirp: a fast spectro-mechanical probe for monitoring transient microstructural evolution of complex fluids during shear. *J. Non-Newtonian Fluid Mech.* 301. <https://doi.org/10.1016/j.jnnfm.2022.104744>
- Ross-Murphy SB (1994) Rheological characterization of polymer gels and networks. *Polym. Gels Netw.* 2(3–4):229–237. [https://doi.org/10.1016/0966-7822\(94\)90007-8](https://doi.org/10.1016/0966-7822(94)90007-8)
- Shannon CE (1949) Communication in the presence of noise. *Proc. IRE* 37(1):10–21
- Sheridan RJ, Zauscher S, Brinson LC (2024) BOTTS: broadband optimized time–temperature superposition for vastly accelerated viscoelastic data acquisition. *Soft Matter* 20:7811–7820. <https://doi.org/10.1039/D4SM00798K>
- TA Instruments (2014) What's new in TRIOS software. Technical report, TA Instruments. Issued October 2014; see p. 6. https://www.tainstruments.com/pdf/NewFeaturesTRIOS_Previous1.pdf
- Totosaus A, Montejano JG, Salazar JA, Guerrero I (2002) A review of physical and chemical protein-gel induction. *Int. J. Food Sci. Technol.* 37(6):589–601. <https://doi.org/10.1046/j.1365-2621.2002.00623.x>
- Trappe V, Weitz D (2000) Scaling of the viscoelasticity of weakly attractive particles. *Phys. Rev. Lett.* 85(2):449. <https://doi.org/10.1103/PhysRevLett.85.449>
- Winter HH, Chambon F (1986) Analysis of linear viscoelasticity of a crosslinking polymer at the gel point. *J. Rheol.* 30(2):367–382. <https://doi.org/10.1122/1.550825>
- Wilhelm M (2002) Fourier-transform rheology. *Macromol. Mater. Eng.* 287(2):83–105. [https://doi.org/10.1002/1439-2054\(20020201\)287:2<83::AID-MAME83>3.0.CO;2-B](https://doi.org/10.1002/1439-2054(20020201)287:2<83::AID-MAME83>3.0.CO;2-B)
- Zaccarelli E (2007) Colloidal gels: equilibrium and non-equilibrium routes. *J. Phys.: Condens. Matter* 19(32). <https://doi.org/10.1088/0953-8984/19/32/323101>

Publisher's Note Springer Nature remains neutral with regard to jurisdictional claims in published maps and institutional affiliations.

Springer Nature or its licensor (e.g. a society or other partner) holds exclusive rights to this article under a publishing agreement with the author(s) or other rightsholder(s); author self-archiving of the accepted manuscript version of this article is solely governed by the terms of such publishing agreement and applicable law.